Design of a Low-Crosstalk Sub-Wavelength-Pitch Silicon Waveguide Array for Optical Phased Array

Guangzhu Zhou, Shi-Wei Qu, *Senior Member, IEEE*, Jieyun Wu, and Shiwen Yang, *Fellow, IEEE*

***Abstract*—In this work, a compact sub-wavelength-pitch silicon waveguide array with low crosstalk is proposed and analyzed. The crosstalk is suppressed by periodic silicon nano-blocks symmetrically arranged along the silicon strip waveguides. The silicon nano-blocks are properly designed to work in the resonant region as a high-reflection boundary so that the evanescent fields of the silicon waveguide, which directly contribute to the coupling between waveguides, can be truncated. Meanwhile, the nano-blocks periodically perturb the evanescent fields to form a weak-radiating grating, leading to a millimeter-long effective radiation length required for highly directive optical phased arrays. Simulation results show that the crosstalk between the waveguides in the proposed design is at least 10 dB lower than traditional waveguide array with identical sizes within the 1500–1590 nm bandwidth. Furthermore, the proposed design achieves an effective radiation length up to 1.47 mm, resulting in a theoretical narrow beam width of 0.052°. Combining both the low crosstalk and the long effective radiating length, our design offers a promising platform for high-performance two-dimensional scanning optical phased array with a large field of view and a narrow beam width.**

***Index Terms*—Optical phased arrays (OPAs), low crosstalk, high-reflection boundary.**

I. Introduction

DUE to the rapid development of photonic integrated circuits (PICs), on-chip optical phased arrays (OPAs) have attracted much attention for their rapid and precise beam steering without mechanical actuators. OPAs have seen extensive applications in light detection and ranging (LiDAR) [1], [2], imaging [3], [4], holographic displays [5], and free-space communications [6]. Particularly, integrated silicon photonics platform which is compatible with CMOS fabrication processes enables large-scale chip-based OPAs with significantly low loss and reduced cost [7].

Beam forming and beam steering in chip-based OPAs are achieved by independently controlling the amplitude and phase of elements of an optical antenna array, typically formed by 1-D waveguide grating arrays with uniform emitter spacing. Ideally, aliasing-free beam scanning can be ensured by a half wavelength antenna element pitch [8]. However, strong crosstalk between waveguides occurs when the element pitch in arrays is below one wavelength, preventing the independent phase control over each antenna elements. Although the crosstalk can be mitigated by sacrificing the longitudinal OPA aperture size, i.e., the effective length along the light propagation direction. However, the low resolution caused by the small aperture size is highly unfavorable for many practical applications like LiDAR, automotive systems, in which a fine resolution is always pursued. As a result, the typical element pitch in current OPAs is several micrometers, giving rise to small aliasing-free beam steering ranges [9]–[11]. Therefore, the tradeoff between the steering range and the element pitch has posed a limitation to the development of high-performance OPAs.

To deal with this circumstance, several methods have been investigated which can be categorized into different types depending on the design strategies used. The first kind is the non-uniform-pitch array designs [12], [13], which is widely adopted in microwave phased arrays. For instance, a sparse optical phased array with a scanning range of 50° is achieved in [12], where the minimum element pitch is 4λ to avoid crosstalk between waveguides and the position of each element is optimized to suppress the grating lobes caused by the large element spacing. Two major drawbacks of the sparse array are the higher side lobe level and the reduced power in main lobe as low as 2%, which greatly reduces the available detection range of the OPAs. Besides, many efforts have been devoted into suppressing the crosstalk between waveguides by introducing phase mismatch between waveguides. In [14], [15], subarrays composed of strip waveguides with different sizes are utilized to suppress the waveguide crosstalk, achieving an ideal half-wavelength element spacing. Also, another type of half-wavelength-pitch silicon waveguide array with low crosstalk is proposed in [16]. Two thin silicon strips with same width are asymmetrically placed between waveguides, thus introducing a strong phase mismatch between two adjacent waveguides. In that design, the crosstalk between waveguides remains below -18 dB even for the array length of 1 mm. Furthermore, recently, a low-crosstalk sinusoidal silicon waveguide array has been put forward [17]. The low crosstalk is achieved by manipulating the difference of super-mode propagation constants of the sinusoidal waveguide. However, there are several drawbacks in the existing designs. Firstly, the phase mismatches are introduced by breaking the symmetry of the structures. It means that wavelength scanning is not available in these designs. In addition, a gap size of 27.5 nm in [16] is very challenging for fabrication.

Manuscript received June 16, 2021; revised July 24, 2021; accepted August 4, 2021. Date of publication August 12, 2021; date of current version August 30, 2021. This work was supported in part by the National Natural Science Foundation of China under Grant U20A20165 and in part by the Fundamental Research Funds for the Central Universities under Grant ZYGX2019Z005. *(Corresponding author: Shi-Wei Qu.)*

Guangzhu Zhou, Shi-Wei Qu, and Shiwen Yang are with the School of Electronic Science and Engineering, University of Electronic Science and Technology of China, Chengdu 611731, China (e-mail: 201811022229@std.uestc.edu.cn; shiweiqu@uestc.edu.cn; swnyang@uestc.edu.cn).

Jieyun Wu is with the School of Optoelectronic Science and Engineering, University of Electronic Science and Technology of China (UESTC), Chengdu 611731, China (e-mail: jieyunwu@uestc.edu.cn).

Digital Object Identifier 10.1109/JPHOT.2021.3103392

On the other hand, for high-resolution LiDAR applications, OPAs with ultra-small beam divergence is always pursued. However, due to strong radiation of silicon-based waveguide grating antennas, it is very challenging for such silicon waveguide arrays to achieve narrow beam width. It has been demonstrated that silicon waveguide grating antenna with a 10 nm feature size can merely provide 1 mm propagation length [18]. There are several reports on small beam-divergence OPAs. For example, low-contrast silicon nitride gratings are deposited on silicon waveguide to achieve a relatively low emission rate which in turn gives rise to large aperture and small beam divergence [19]–[21]. In addition, a surface-emitting silicon waveguide antenna with a radiation length of 3.65 mm has been reported [22], in which periodic radiative segments are placed on both sides of a subwavelength metamaterial waveguide to form weak radiating grating. Nevertheless, the coupling between antennas is not considered in that design.

In this paper, we propose a compact sub-wavelength-pitch silicon waveguide array, where one-dimensional periodic blocks are symmetrically arranged along silicon strip waveguides. The periodic structures are the key to achieve low crosstalk simultaneously millimeter-long radiation length. The designs presented in this paper are based on a silicon-on-insulator (SOI) platform and are compatible with CMOS technology. Simulation results show that the crosstalk between waveguides in the proposed design is at least 10 dB lower than the referenced traditional waveguide array with identical sizes within the 1500 $\sim$ 1590 nm bandwidth. Moreover, the one-dimensional periodic structure is introduced without breaking structure symmetry. Hence, the proposed design is capable of wavelength scanning. For the waveguide array with an element pitch of 1 μm in this design, overall aliasing-free beam steering ranges of 100° can be achieved with the phase modulation method and 19.3° beam steering ranges via wavelength tuning by 113 nm is numerically demonstrated. Furthermore, the proposed design achieves an effective radiation length up to 1.47 mm, corresponding to a theoretical narrow beam width of 0.052°. Therefore, our design offers a promising platform for realization of two-dimensional scanning optical phased array with a large field of view and a narrow beam width.

II. Design and Result

A. Crosstalk Reduction

The schematic views of the proposed structure are shown in Figs. 1(a) and 1(c). To illustrate the operating principle, the crosstalk of the proposed two-waveguide system is investigated and compared to that of conventional design shown in Figs. 1(b) and 1(d) as a reference. The insets in (a) and (c) show the cross-section of the proposed two-waveguide system and the referenced one, respectively. In our design, one-dimensional (1-D) periodic nano-blocks with a period Λ are symmetrically placed along the two strip waveguides. The silicon nano-blocks are with a width b and a length a. The two strip waveguides, with a center-to-center distance D, have the same width W and height H. The periodic silicon nano-blocks and the silicon strip waveguides are separated by a gap G. According to the coupled mode theory, for the reference conventional two-waveguide system, symmetric and antisymmetric modes with the propagation constants of β_+ and β_- will be simultaneously excited when light is launched

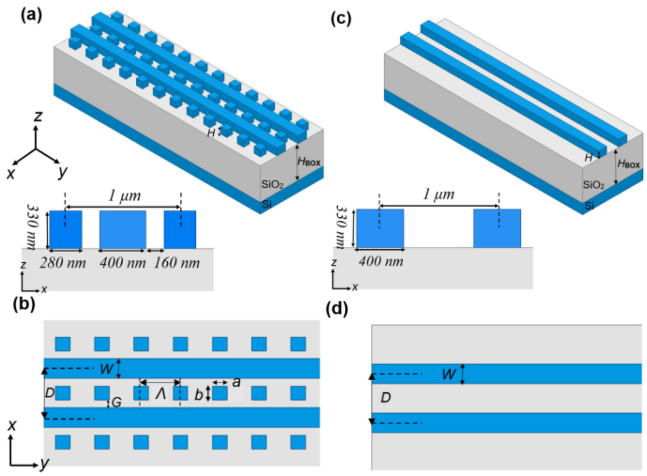

Fig. 1. 3D schematic views (a) of the proposed structure and (b) the referenced conventional two-waveguide system. Top views of (c) the proposed structure and (d) the referenced conventional two-waveguide system. The insets in (a) and (c) shows the cross-section of the proposed structure and the referenced one. The insets in (a) and (c) show the cross-section of the proposed two-waveguide system and the referenced one.

from one waveguide. When the two modes propagate along the waveguides, if the accumulated phase difference between them reaches π, the energy in the input waveguide will be transferred into the other one to the maximum extent. The crosstalk can be expressed as [16]:

$$\frac{P_{1\to2}}{P_1} = F\sin^2\left(\frac{\pi L}{2L_C(\lambda)}\right) \tag{1}$$

where P_1 and $P_{1\to2}$ are the input power in the input waveguide and the transferred power from the input waveguide to the other one, respectively. F, L and L_C represent the maximum crosstalk, the propagation length and the coupling length, respectively. Generally, $F = 1$ is reached when the propagating length L equals the coupling length L_C, and it always holds for the referenced lossless two-waveguide system shown in Figs. 1(c) and 1(d). It means the energy in the input waveguide is completely transferred to the other. In addition, the material dispersion or wavelength dependence may result in the difference in coupling length L_C of traditional two-waveguide system, but the maximum crosstalk F will not be changed.

On the other hand, according to the total internal reflection mechanism of the optical dielectric waveguide, the dispersion relation can be described as [23]:

$$\frac{(k_y)^2}{\varepsilon_x} + \frac{(k_x)^2}{\varepsilon_y} = (k_0)^2 \tag{2}$$

where k_0 is free-space wavenumber, k_y and k_x are the wavenumber along the longitudinal direction and the transverse direction of the waveguide in our case. ε_x and ε_y represent the anisotropic dielectric constant along the x- and y-axis, respectively.

Particularly, it is the evanescent waves decaying along waveguide-transverse direction that directly contribute to the coupling between waveguides. Therefore, it has been demonstrated that the coupling length L_C can be effectively extended by utilizing highly anisotropic photonic metamaterial to tailor the evanescent waves [24]–[26]. In our design, the 1-D periodic silicon nano-blocks are utilized as high-reflection boundaries

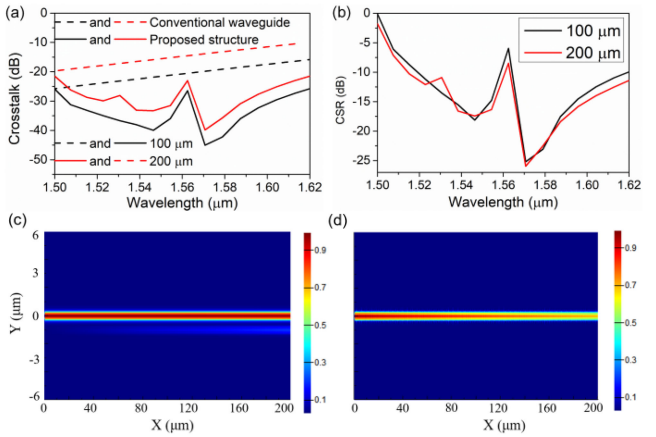

Fig. 2. With different waveguide lengths of 100 μm and 200 μm, (a) the crosstalk of the proposed design and the referenced two-waveguide system, and (b) the corresponding CSR. The normalized *E*-field distributions of (c) referenced two-waveguide system, and (d) the proposed design.

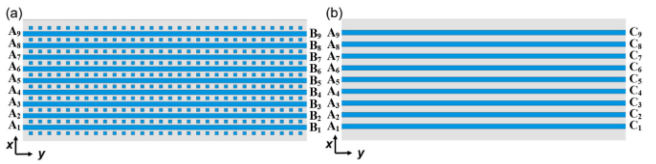

Fig. 3. Top views of (a) the proposed waveguide array, and (b) the referenced waveguide array. The input ports are uniformly numbered from A_1 to A_9, and all output ports in the two arrays are numbered, individually.

to harness the evanescent waves of the silicon strip waveguides. The parameters of the silicon nano-blocks are properly designed to make the 1-D periodic structures work in their resonant regions, so that the energy of the evanescent waves will be truncated by the periodic structures. As a result, low crosstalk between the waveguides can be achieved. Accordingly, the crosstalk of the proposed design is rewritten as follows:

$$\frac{P_{1\to 2}}{P_1} = F(\lambda)\sin^2\left(\frac{\pi L}{2L_C(\lambda)}\right) \tag{3}$$

It means the maximum crosstalk F become a function of wavelength resulting from the resonant characteristics of the 1-D periodic structures.

To validate the effectiveness of our design, a pair of low-crosstalk waveguides with $D = 1$ μm are designed. The length a, width b and period Λ of the silicon nano-blocks are 300 nm, 280 nm, and 800 nm, respectively. Their overall height H is optimized to be 330 nm, and the width W is set as 400 nm for transverse-electric (TE) single-mode operation. Therefore, in this design, a relatively large feature size $G = 160$ nm is reserved for ease of fabrication. Although a nonstandard silicon thickness of 330 nm is employed in the calculations to demonstrate the crosstalk reduction, the same approach to minimize crosstalk can be achieved in standard 300 nm platform and commercial 340 nm platform (which is discussed in Fig. 8(c)). The proposed two-waveguide systems with the propagation lengths of 100 μm and 200 μm are simulated, respectively. Besides, the referenced two-waveguide system with identical waveguide sizes is also simulated for comparison purpose. The simulations are carried out using software package, e.g., Empire 8.04, which

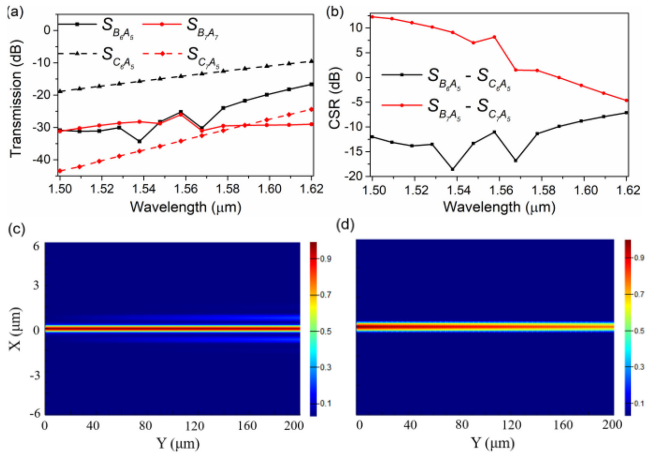

Fig. 4. (a) With the waveguide lengths of 200 μm, the simulated transmission spectrums of the conventional waveguide array and the proposed design. (b) The corresponding CSR. The corresponding normalized *E*-field distributions of (c) the conventional waveguide array, and (d) the proposed waveguide array, at the wavelength of 1.55 μm. The input ports in both waveguide arrays are set to port A_5. The parameters employed in these calculations are: $W = 400$ nm, $H = 330$ nm, $G = 160$ nm, $a = 300$ nm, $b = 280$ nm, and $\Lambda = 800$ nm, respectively.

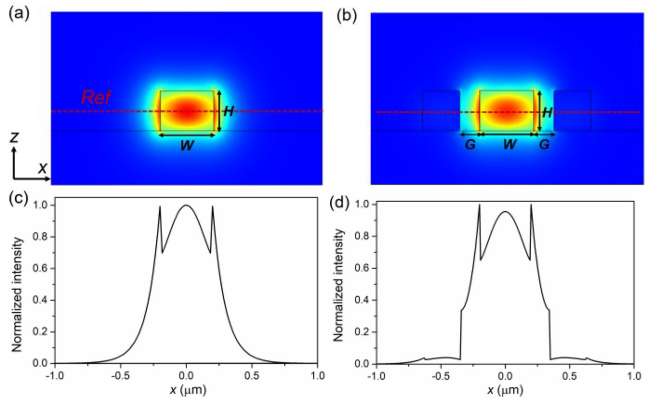

Fig. 5. The TE-eigenmode field distributions of (a) a conventional strip waveguide, and (b) the evanescent-field modulated strip waveguide. The normalized *E*-field intensity along the reference line (red dash line) of (c) a conventional strip waveguide, and (d) the evanescent-field modulated strip waveguide. The parameters are: $W = 400$ nm, $H = 330$ nm, $G = 160$ nm.

is based on the finite-different time-domain (FDTD) method. In the simulations, PML absorption boundaries are applied to absorb outgoing waves and simulate the open space. Wave ports are added to excite the fundamental TE mode of the silicon strip waveguide and calculate the transmission or crosstalk in arrays. The refraction indices of SiO_2 and Si are 1.444 and 3.48 in these calculations, respectively. The cladding of the arrays presented in this paper is air. In the calculations, a TE-polarized wave is launched into the single-mode waveguide with a width and height of 400 nm and 330 nm, respectively. After traveling through a short transmission region, it propagates into the radiation region where 1-D periodic structures are arranged on both of the waveguide to radiate the energy into free space and simultaneously to suppress the crosstalk between waveguides.

Fig. 2(a) shows the crosstalk between waveguides for both the referenced two-waveguide system and the proposed design. As indicated by the dash curves in Fig. 2(a), for the conventional design, the crosstalk between waveguides varies linearly with

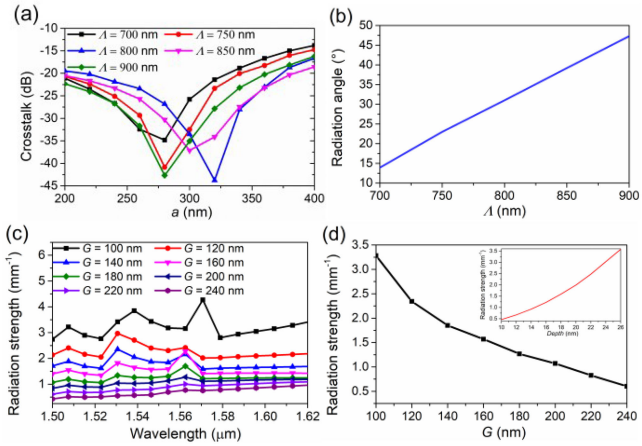

Fig. 6. (a) The crosstalk versus the length a in different period of the periodic silicon blocks at the operating wavelength of 1550 nm. (b) Radiation angle of the evanescent-field-modulated grating antennas as a function of the period of the 1-D periodic structure at 1550 nm. (c) The radiation strength as a function of operating wavelength at different gap size G. (d) Radiation strength as a function of gap size G. The inset in (d) shows the radiation strength versus the perturbed depth of conventional waveguide grating antenna with the same waveguide parameters of width W and height H. The parameters are: $W = 400$ nm, $H = 330$ nm, $G = 160$ nm, $a = 300$ nm, $b = 280$ nm, and $\Lambda = 800$ nm, respectively.

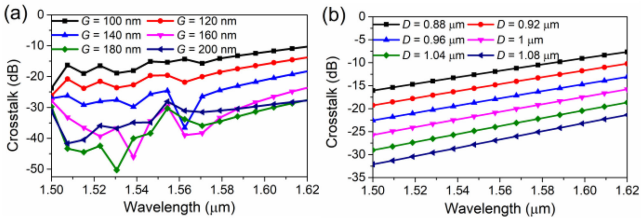

Fig. 7. (a) Crosstalk as a function of wavelength at different gap size G for the proposed structure. (b) Crosstalk versus wavelength at different waveguide pitch D for a conventional two-waveguide system.

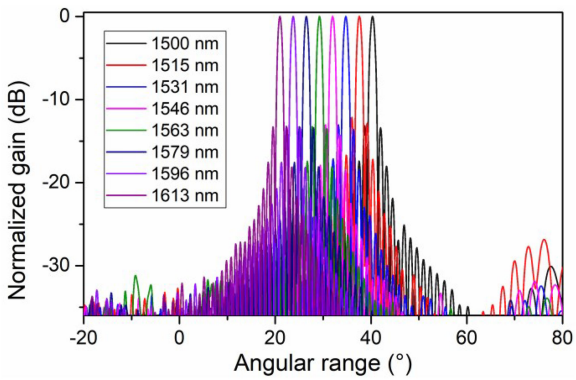

Fig. 8. Normalized far-field gain patterns at various wavelengths.

wavelength. As a comparison, in our design, as indicated by the solid curves in Fig. 2(a), the crosstalk is greatly suppressed when introducing the 1-D periodic structures, even for such a long propagation length of 200 μm (about 129λ). To show the coupling suppression effect more intuitively, the coupling suppression ratio (CSR), defined as the coupled energy ratio between the proposed design and the referenced one under the same propagation length, is shown in Fig. 2(b). It can be seen that within the 1500–1620 nm wavelength ranges, the crosstalk of the proposed design is lower than that of the referenced one. The maximal CSR reaches up to 25 dB at the wavelength of 1.57 μm. Ideally, the CSR does not vary with the propagating length because of the intrinsic resonant characteristics of the periodic structures. However, the crosstalk suppression becomes better with the increasing of propagation length due to the weak-radiating grating radiation formed by the periodically arranged silicon nano-blocks. This phenomenon is verified in Fig. 2(b), where the CSR of two waveguide lengths of 100 μm and 200 μm are illustrated, respectively. The corresponding normalized E-field distributions of the referenced two-waveguide system and the proposed design at the wavelength of 1.55 μm are depicted in Figs. 2(c) and 2(d), respectively.

Above discussions indicate that, for the proposed two-waveguide systems, the crosstalk can be effectively suppressed via evanescent field manipulation, giving rise to a very small coupling coefficient F. When extended to waveguide array case, the coupling paths become more complicated [27]. Taking a three-waveguide system as an example, two dominant coupling paths need to be considered. In the first case, the couplings originate directly from the input waveguide. When light is launched from one waveguide, the energy will be coupled into the waveguides nearby with the coupling strength decays with the distance from the input waveguide. The second coupling path involves the coupling from the nearest waveguide to the next-nearest waveguide. According to the above analysis about the proposed two-waveguide system, the crosstalk between adjacent waveguides can be effectively suppressed by introducing the 1-D periodic structures. On the other hand, a 2 μm distance between the input waveguide and the next-nearest waveguide in our case is sufficient to suppress the coupling from the input waveguide to the next-nearest waveguide. Therefore, a sub-wavelength pitch silicon waveguide array with low crosstalk can be obtained.

Based on the given parameters of the proposed two-waveguide system, a silicon waveguide array is constructed to demonstrate the crosstalk suppression effect of our design. The top view of the proposed waveguide array is shown in Fig. 3(a). Meanwhile for comparison purpose, a reference waveguide array with identical physical parameters is also simulated as shown in Fig. 3(b). The array lengths are 200 μm and number of the waveguides in both arrays is set to be 9, which is sufficient to investigate the couplings of a waveguide array. As shown in Figs. 3(a) and 3(b), the input ports are uniformly numbered from A_1 to A_9, and each output port on the right side is individually numbered to distinguish from the others.

Fig. 4(a) give the simulated coupling coefficients for both the proposed and the referenced waveguide arrays when light is launched from the center waveguide, i.e., Port A_5 for both arrays. In Fig. 4(a), S_{C6A5} and S_{C7A5} represent the energy coupling coefficients from Port A_5 to Port C_6 and C_7 in the referenced waveguide array, respectively. Similar case holds for S_{B6A5} andS_{B7A5} in the proposed design. Because two major coupling paths, i.e., one from the input waveguide to the nearest waveguides and the other one to the next-nearest waveguides, dominate the couplings, while energy coupling via other coupling paths are negligible, the coupling between Port A_5 and the nearest two waveguides are our major concerns, i.e., S_{B6A5}/S_{B4A5} and S_{B7A5}/S_{B3A5}. In addition, the symmetry of the structures, makes the fields symmetrically distributed

with respect to the input waveguide. It means $S_{B6A5} = S_{B4A5}$ and $S_{B7A5} = S_{B3A5}$. Therefore, for the proposed design, only S_{B6A5} and S_{B7A5} are illustrated for the sake of brevity. Similarly, for the referenced waveguide array, the corresponding parameters S_{C6A5} and S_{C7A5} are illustrated in Fig. 4(a) by dash curves for comparison purpose. It can be seen that for the referenced waveguide array, the maximum coupling occurs at the wavelength of 1.62 μm, where up to 22% of the input power is transferred into the two adjacent waveguides. However, in the proposed design, the couplings to adjacent waveguides are effectively suppressed owning to the introduction of the 1-D periodic structures, which are negligible compared to those in the referenced waveguide array. A CSR with respect to the adjacent waveguides of over 10 dB is achieved within the wavelength ranges of 1.5–1.59 μm as shown in Fig. 4(b). Compared with the proposed two-waveguide system results shown in Fig. 2(b) and the waveguide array results shown in Fig. 4(b), the CSR in the waveguide array case is slightly lower than that in the two-waveguide system analyzed above due to more complicated coupling paths and the array environment impacts in the array case. However, the 1-D periodic silicon nano-blocks can be further optimized in the array environment for higher CSR. Furthermore, for the coupling from input waveguide to the next-nearest waveguide, e.g., from Port A_5 to Port B_7, without special engineering, the structures between the two waveguides have no effect on coupling suppression. Comparatively, the introduced 1-D periodic structure increases the coupling from the input waveguide to the next-nearest waveguide, as indicated by the red curve in Fig. 4(a), resulting in a positive CSR over a large wavelength range. However, in the proposed deign, the crosstalk to the next-nearest waveguide still maintains at a low level, e.g., below -27 dB as shown in Fig. 4(a), due to the relatively large waveguide pitch of 2 μm between the input waveguide and the next-nearest waveguide. Figs. 4(c) and 4(d) depict the normalized *E*-field distribution of the referenced waveguide array and the proposed design at the wavelength of 1.55 μm. For the referenced waveguide array, the energy launched from Port A_5 into the input waveguide is gradually coupled to other waveguides inside the array. Comparatively, in the proposed design, as seen in Fig. 4(d), crosstalk is barely observed when light is launched from the center waveguide. In addition, the electric fields in the input waveguide gradually decays along the wave propagating direction due to the grating radiation caused by the periodically arranged silicon nano-blocks. Similar *E*-field distributions can be obtained by launching power into other waveguides. Accordingly, low-crosstalk silicon waveguide arrays with a large number of waveguides can also be achieved. Therefore, our design holds a great promise for larger-scale integrated OPAs.

B. Radiation Rates and Frequency-Scanning Characteristics

In this section, the radiation characteristics of the proposed structure are discussed. Different from conventional sidewall-modulated waveguide grating antennas, in this design, the radiation grating is formed by periodical perturbation of the silicon nano-blocks to the evanescent fields of the silicon strip waveguides. For referenced silicon strip waveguide, the field distribution of TE-eigenmode is shown in Fig. 5(a). When silicon blocks are arranged on both sides of the strip waveguide and separated from the waveguide with a gap *G*, the TE-eigenmode field distribution is shown in Fig. 5(b). In addition, the normalized *E*-field intensity distributing along the red reference lines are illustrated in Figs. 5(c) and 5(d), respectively. It can be seen that partial evanescent field is perturbed by the silicon nano-blocks. With properly designed parameters of the silicon nano-blocks and the gap *G*, the evanescent field can be modulated accordingly. When the period of the 1-D periodic structure is comparable with the waveguide wavelength in the silicon strip waveguide, the radiating grating is formed and light will be radiated out. Compared with conventional sidewall-modulated waveguide grating antennas where a small feature size leads to strong radiation, the evanescent-field-modulated grating antennas allow a relatively large feature size to achieve weak radiation rate.

Identical to traditional gratings, the radiation angle of the proposed structure is decided by the following grating equation [1]:

$$\sin\theta = \frac{n_{eff}\Lambda - \lambda_0}{\Lambda} \tag{4}$$

where θ is the radiation angle, which depends on the effective refractive index n_{eff} of the grating, the period Λ of the 1-D periodic structure and the free-space wavelength λ_0 (for the case of air cladding in our case).

In the proposed design, the 1-D periodic structures are the key to radiate energy into free space and achieve low crosstalk between waveguides at the same time. Therefore, the impacts of the length *a* and period Λ of the periodic silicon nano-blocks on crosstalk between waveguides and antenna radiation characteristics are investigated, respectively. At the 1.55 μm wavelength, the crosstalk versus silicon nano-block length *a* at different period Λ are shown in Fig. 6(a), which are derived from the proposed two-waveguide system shown in Fig. 1(a). It can be seen that for different period Λ, optimal crosstalk suppression can always be obtained by properly arranging the duty cycle (defined as a/Λ) of the 1-D periodic structure. On the other hand, generally, the radiation direction is designed at an angle to the normal of chip surface to reduce the back-reflection intensity [28]. Here, the radiation angle versus the period Λ is illustrated in Fig. 6(b), in which $b = 300$ nm and keep unchanged. Therefore, for the proposed design, the radiation angle can be designed by properly arranging the period of the silicon nano-blocks and the crosstalk suppression can be achieved by optimizing the parameters of the silicon nano-blocks of the 1-D periodic structure, i.e., width *b* and length *a*.

Another key aspect of this design is the radiation strength α, which is defined as the required propagating length to radiate 99% of the input power, can be substantially reduced with the increasing of the gap size *G*. When light propagates in the evanescent-field modulated silicon strip waveguide, due to the grating radiation, the E-field intensity will decay exponentially with the propagating length. Therefore, the radiation strength α can be calculated by $P_{out} = P_{in}\ exp(-2\alpha L)$, where P_{in} and P_{out} are the power launched into the input waveguide and the remaining power with light propagating in the waveguide by a length *L*, respectively.

Within the $1.5 \sim 1.62$ μm wavelength ranges, the radiation strength at different gap sizes *G* is shown in Fig. 6(c). In order to illustrate the influence of gap size on radiation strength more intuitively, the radiation strength as a function of gap

TABLE 1
THE CORRESPONDING WAVEGUIDE PITCH *D* AT DIFFERENT GAP SIZE *G*

G	0.1	0.12	0.14	0.16	0.18	0.2	(μm)
D	0.88	0.92	0.96	1	1.04	1.08	(μm)

size *G* is shown in Fig. 6(d). As indicated by Fig. 5(c), the evanescent fields will gradually decay when away from input waveguide. Therefore, the larger the gap size is, the weaker the perturbation of the silicon nano-blocks to the evanescent fields of the silicon strip waveguide will be. As a result, radiation strength is dramatically reduced with the increasing of the gap size *G* as indicated in Fig. 6(d). Comparatively, for conventional waveguide grating antenna with identical physical parameters, the radiation strength as a function of perturbed depth is shown in the inset of Fig. 6(d). It can be seen that although a relatively large minimal feature size *G* is adopted in the proposed design, the radiation strength is comparable to the referenced conventional waveguide grating antenna with the perturbed depth of a dozen nanometers. Moreover, as seen in Fig. 6(c), the radiation strength shows a smaller fluctuation in the wavelength domains with the increasing of gap size *G*, which is very favorable for OPAs to achieve two-dimensional scanning with stable angular resolution in the far-field region. However, a larger gap size *G* means a larger element pitch, resulting in smaller aliasing-free beam steering ranges of OPAs.

Therefore, in the proposed design, the gap size *G* is designed to be 160 nm for a tradeoff between the radiation strength and steering range. At the 1.55 μm wavelength, a weak radiation strength α about 1.57 mm^{-1} is obtained under the radiation angle of 31.4°. To radiate 99% of the input power, the corresponding radiation length is about 1.47 mm. According to [29], the 3-dB beamwidth of 1-D leaky-wave antennas is given as follows:

$$\Delta\theta_{3dB} \approx \frac{2\alpha}{k_0 \cos(\theta)} \tag{5}$$

where α, k_0 and θ are radiation strength, free-space wavenumber and radiation angle, respectively. The radiation length of 1.47 mm yields a corresponding 3-dB beamwidth of 0.052° in the far-field region at the wavelength of 1.55 μm. Such narrow beam width is very favorable for automotive LiDAR applications where an angular resolution around 0.1° is required for distinguishing any potential hazards even at a distance of 200 m [30], [31].

Although the sizes of periodic silicon blocks play a crucial role in coupling suppression, the gap size *G* will also have significant effects. Therefore, in the proposed two-waveguide system, the crosstalk as a function of wavelength at different *G* is given in Fig. 7(a). It is worth noting that varying *G* and keeping *b* a constant at the same time, the waveguide pitch *D* will also change. For a fair comparison, in the conventional two-waveguide system, the crosstalk versus wavelength at various *D* is presented in Fig. 7(b). The corresponding relationships between *D* and *G* are shown in Table 1. As shown in Fig. 7(a), with the increasing of *G*, the resonant characteristics gradually emerges. Besides, in the proposed design, when *G* is larger than 160 nm, no obvious improvement in coupling suppression can be observed. Therefore, *G* is also optimized to be 160 nm for a tradeoff between the crosstalk suppression effect and element pitch.

On the other hand, in the previous reports [14]–[17], large phase mismatches are introduced with asymmetric structures to suppress the crosstalk between waveguides. Due to different dispersion relationships of antenna elements, the wavelength scanning will be infeasible in these designs. However, in the proposed design, the 1-D periodic silicon nano-blocks are introduced without breaking the structure symmetry, making the proposed waveguide array available for wavelength scanning besides low crosstalk between waveguides and weak radiation strength. With the waveguide length of 200 μm, the normalized far-field gain patterns at various wavelengths are shown in Fig. 8. For wavelength ranging from 1500 to 1613 nm, the radiation angle varies from 40.3° to 21°, corresponding to a tuning efficiency of 0.17°/nm. According to the antenna theories, the scanning angle θ can be expressed as follows [32]:

$$\theta = \sin^{-1}\left(\frac{m \times 2\pi + \Delta\phi}{2\pi} \times \frac{\lambda}{D}\right) \tag{6}$$

Where $\Delta\Phi$, λ, *D* are the phase difference between adjacent antenna element, free-space wavelength and element pitch, respectively and *m* is an integer. To avoid the grating lobes, a single real solution is required in Eq. (3) for all m $\geq$ 1:

$$\left|\frac{m \times 2\pi + \Delta\Phi}{2\pi} \times \frac{\lambda}{D}\right| > 1 \tag{7}$$

It indicates that aliasing-free beam scanning can be ensured by the antenna element pitch below half a wavelength. However, limited by the crosstalk in optical waveguide arrays, the element pitch is typically larger than half a wavelength. Therefore, the first grating lobe appears at $m = \pm 1$. In addition, the aliasing-free beam steering ranges can be theoretically calculated according to (8). At the wavelength of 1.55 μm, for the waveguide array with an element pitch of $D = 1$ μm in this design, an overall aliasing-free beam steering range of around 100° can be achieved with the phase modulation method [10].

$$2\theta = 2\arcsin\left(\frac{\lambda}{2D}\right) \tag{8}$$

To verify the beam-steering characteristics by the phase modulation method, a uniform linear array composed of 20 ideal point sources and spacing with an identical element pitch of 1 μm is theoretically calculated. The corresponding far-field radiation patterns at various angles are illustrated in Figs. 9(a)–(d). It can be seen from Fig. 9(c), when scanning up to 33°, the first grating lobe appears at $-90°$. Besides, when it scans up to 50°, the first grating lobe appears at $-50°$, indicating an over field of view of 100° as illustrated in Fig. 9(d). These results are in good agreement with the theoretical calculations.

Table 2 gives the summary and comparisons with prior beam-steering OPAs on the performances, e.g., array element pitch, field of view, beam divergence and crosstalk. It should be noted that the beam divergence in transverse direction (waveguide array direction) exactly depends on the number of the antenna element and more antenna element leads to smaller beam divergence angle, while the beam divergence in longitude direction (light propagating direction) depends on the effective radiating length of the grating. The mutual restraints between array element pitch and field of view pose a limitation to the

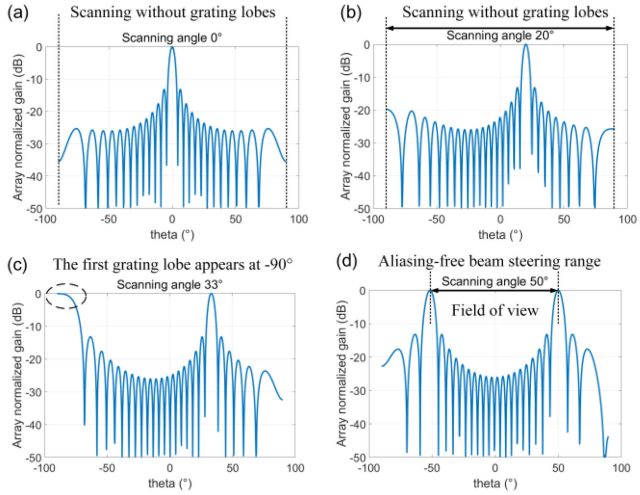

Fig. 9. For a uniform linear array composed by 20 ideal point sources and spacing with an identical element pitch of 1 μm with the proposed structure, the far-field radiation patterns at the scanning angles of (a) 0°, (b) 20°, (c) 33°, and (d) 50°.

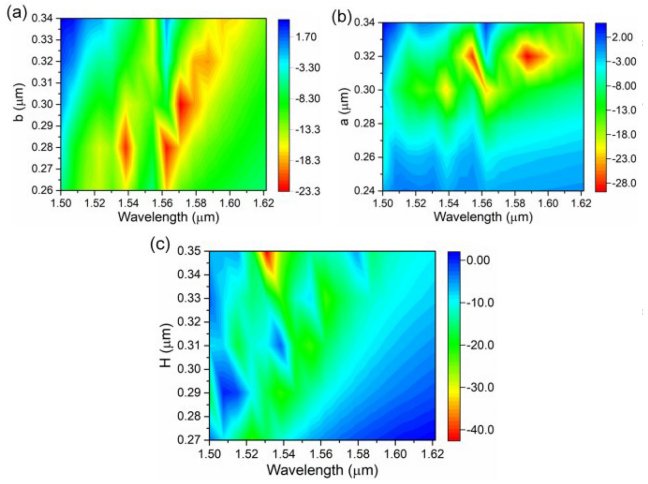

Fig. 10. The CSR versus wavelength at different (a) width b and (b) length a of the periodic silicon nano-blocks, and (c) overall height H of the proposed design.

TABLE 2
SUMMARY AND COMPARISONS WITH PRIOR BEAM-STEERING OPAS

Year and Ref.	Array pitch and field of view	Beam divergence and crosstalk
2011 [1]	3.5 μm / 20° × 14°	0.6° × 1.6° / NA
2014 [9]	4 μm / 20° × 15°	1.2° × 0.5° / NA
2017 [2]	2 μm / 46° × 36°	0.85° × 0.18° / NA
2019 [33]	20 μm / 6.6° × 4.4°	0.042° × 0.031° / NA
2019 [19]	1.3 μm / 70° × 3.3°	N/A / below -12 dB
2021 [34]	2 μm / 104° × 17.6°	0.72° × 1.74° / NA
2021 [35]	800 nm / 180° (1D)	N/A / below -20 dB
This work	1 μm / 100° × 19.3°	0.052° / below -10 dB

development of high-performance OPAs. Therefore, reducing the element pitch while keeping a low crosstalk between antenna elements can substantially extend the scanning angle of OPAs.

In the simulations, the beam steering can be achieved by individually controlling the phase of each input port. However, in an experimental system of OPA, MMI splitters are required to split the input power into N channels, followed by a phase-modulated region and the designed waveguide grating antennas. The phase in the phase-modulated region can be modulated via thermo-optic effect or plasma dispersion effect [36]. The phase shifters based on thermo-optic effect generally suffer from high power consumption. For example, a heating power of 22 mW is required for 2π phase shift. Compared with the thermo-optic phase shifters, although the phase shifters based on plasma dispersion effect can provide smaller power consumption and faster response, optical loss is unavoidable in these devices. As examples, additional losses for the 2π electro-optic phase shift presented in [37] and [38] are about 2.9 $\sim$ 3.2 dB and 6 dB, and the tuning powers are about 3.4 mW/2π and 4.6 mW/2π, respectively.

III. FABRICATION TOLERANCE

The proposed design with the minimum feature size $G = 160$ nm can be fabricated using single-step electron beam lithography and etching processes, which simplifies the fabrication. In this section, the fabrication tolerances of the proposed design are investigated and the impacts of the fabrication errors on the crosstalk fluctuation are our primary consideration. Figs. 10(a)–10(c) show the CSR within the wavelength ranges of 1.5 $\sim$ 1.62 μm at different width b, length a and height H of the periodic silicon nano-blocks, respectively.

It can be seen that the width b has a significant influence on the resonant frequencies of the 1-D periodic structure. As mentioned above, the evanescent waves of the silicon strip waveguide contribute to the coupling between waveguides. When the evanescent wave propagates along the x- direction with a wave vector k_x, the parameter b will play a decisive role in the traveling path that the energy transfers from the input waveguide to adjacent ones. Therefore, the resonant frequencies of the periodic structure are directly influenced by parameter b. As seen in Fig. 10(a), with the increasing of b, the two resonances are both shifted downwards to lower frequencies because of the increased traveling path, resulting in deterioration of the CSR at high frequencies. As indicated by Fig. 6(a), when keeping the period Λ a constant, the duty cycle can be properly designed to obtain optimal crosstalk suppression between waveguides. It can be seen from Fig. 10(b), the CSR is hardly influenced under a reasonable deviation of fabrication errors of the silicon nano-block length a. In addition, the resonant frequencies are affected by the structure overall height H. With the decreasing of height H, the CSR at low frequencies will slightly deteriorate. Considering that the proposed design can be fabricated with the electron beam lithography process, generally, the size deviations of the structure are on the order from a few nanometers to a few dozens of nanometers. As shown in Figs. 10(a)-10(c), the crosstalk can be suppressed well over a large wavelength range even when the fabrication error is as large as $\pm$ 20 nm. Therefore, these results strongly suggest that the proposed design holds considerable merit in favorable fabrication tolerances.

IV. CONCLUSION

In this paper, a compact sub-wavelength-pitch silicon waveguide array for OPAs is proposed. Firstly, a pair of waveguides

with element pitch of 1 μm are analyzed and discussed to illustrate the operating principle of the proposed design. Then, a low crosstalk waveguide array is structured based on the given parameters of the proposed two-waveguide system. Simulation results show that within the 1500 $\sim$ 1590 nm bandwidth, the crosstalk between the waveguides in the proposed design is at least 10 dB lower than the referenced traditional waveguide array with identical physical parameters. Furthermore, the silicon blocks periodically perturb the evanescent fields of the silicon strip waveguide forming weak radiating grating. Therefore, the radiation characteristics of the evanescent-field modulated waveguide grating are investigated. It demonstrates that the proposed design achieves an effective radiation length up to about 1.47 mm at the wavelength of 1.55 μm. As a result, a theoretical narrow beam width of 0.052° is achieved in the far field. For the waveguide array with an element pitch of 1 μm in this design, theoretical aliasing-free beam steering ranges of 100° can be achieved with phase modulation method. Overall 19.3° beam steering ranges via wavelength tuning by 113 nm, corresponding to the tuning efficiency of 0.17°/nm, is numerically demonstrated. Finally, the fabrication tolerances of the proposed design are investigated. Our results indicate that the design is robust to reasonable fabrication errors from parameter variations of the 1-D periodic silicon nano-blocks. Therefore, the proposed waveguide array will be very promising in realizing high-performance two-dimensional scanning OPAs of the solid-state LiDAR with a large field of view and a narrow beam width.

REFERENCES

[1] J. K. Doylend, M. J. R. Heck, J. T. Bovington, J. D. Peters, L. A. Coldren, and J. E. Bowers, "Two-dimensional free-space beam steering with an optical phased array on silicon-on-insulator," *Opt. Exp.*, vol. 19, no. 22, pp. 21595–21604, Oct. 2011.

[2] C. V. Poulton *et al.*, "Coherent solid-state LIDAR with silicon photonic optical phased arrays," *Opt. Lett.*, vol. 42, no. 20, pp. 4091–4094, Oct. 2017.

[3] Y. Kohno, K. Komatsu, R. Tang, Y. Ozeki, Y. Nakano, and T. Tanemura, "Ghost imaging using a large-scale silicon photonic phased array chip," *Opt. Exp.*, vol. 27, no. 3, pp. 3817–3823, Feb. 2019.

[4] J. Sun, E. Timurdogan, A. Yaacobi, E. S. Hosseini, and M. R. Watts, "Large-scale nanophotonic phased array," *Nature*, vol. 493, no. 7431, pp. 195–199, Jan. 2013.

[5] G. Yang, W. Han, T. Xie, and H. Xie, "Electronic holographic three-dimensional display with enlarged viewing angle using non-mechanical scanning technology," *OSA Continuum,* vol. 2, no. 6, pp. 1917–1924, Jun. 2019.

[6] W. M. Neubert, K. H. Kudielka, W. R. Leeb, and A. L. Scholtz, "Experimental demonstration of an optical phased array antenna for laser space communications," *Appl. Opt.*, vol. 33, no. 18, pp. 3820–3830, Jun. 1994.

[7] C. Hulme *et al.*, "Fully integrated hybrid silicon two-dimensional beam scanner," *Opt. Exp.*, vol. 23, no. 5, pp. 5861–5874, Mar. 2015.

[8] G. Zhou, S. W. Qu, and J. Wu, "Grating lobe suppression in optical phased arrays by loading near-wavelength grating," *Opt. Lett.*, vol. 45, no. 20, pp. 5664–5667, Oct. 2020.

[9] D. Kwong *et al.*, "On-chip silicon optical phased array for two-dimensional beam steering," *Opt. Lett.*, vol. 39, no. 4, pp. 941–944, Feb. 2014.

[10] T. Kim *et al.*, "A single-chip optical phased array in a wafer-scale silicon photonics/CMOS 3D-integration platform," *IEEE J. Solid-State Circuits*, vol. 54, no. 11, pp. 3061–3074, Nov. 2019.

[11] S. M. Kim, T. H. Park, C. S. Im, S. S. Lee, T. Kim, and M. C. Oh, "Temporal response of polymer waveguide beam scanner with thermo-optic phased-modulator array," *Opt. Exp.*, vol. 28, no. 3, pp. 3768–3778, Feb. 2020.

[12] D. N. Hutchison *et al.*, "High-resolution aliasing-free optical beam steering," *Optica*, vol. 3, no. 8, pp. 887–890, Aug. 2016.

[13] R. Fatemi, A. Khachaturian, and A. Hajimiri, "A nonuniform sparse 2-D large-FOV optical phased array with a low-power PWM drive," *IEEE J. Solid-State Circuits*, vol. 54, no. 5, pp. 1200–1215, May 2019.

[14] W. Song *et al.*, "High-density waveguide superlattices with low crosstalk," *Nat. Commun.*, vol. 6, no. 1, pp. 7027, May 2015.

[15] R. Gatdula, S. Abbaslou, M. Lu, A. Stein, and W. Jiang, "Guiding light in bent waveguide superlattices with low crosstalk," *Optica*, vol. 6, no. 5, pp. 585–591, May 2019.

[16] L. Wang *et al.*, "Design of a low-crosstalk half-wavelength pitch nano-structured silicon waveguide array," *Opt. Lett.*, vol. 44, no. 13, pp. 3266–3269, Jul. 2019.

[17] X. Yi, H. Zeng, S. Gao, and C. Qiu, "Design of an ultra-compact low-crosstalk sinusoidal waveguide array for optical phased array," *Opt. Exp.*, vol. 28, no. 25, pp. 37505–37513, Dec. 2020.

[18] H. Xu and Y. Shi, "Diffraction engineering for silicon waveguide grating antenna by harnessing bound state in the continuum," *Nanophotonics*, vol. 9, no. 6, pp. 1439–1446, 2020.

[19] Y. Zhang *et al.*, "Sub-wavelength-pitch silicon-photonic optical phased array for large field-of-regard coherent optical beam steering," *Opt. Exp.*, vol. 27, no. 3, pp. 1929–1940, Feb. 2019.

[20] K. Shang *et al.*, "Uniform emission, constant wavevector silicon grating surface emitter for beam steering with ultra-sharp instantaneous field-of-view," *Opt. Exp.*, vol. 25, no. 17, pp. 19655–19661, Aug. 2017.

[21] M. Zadka, Y. C. Chang, A. Mohanty, C. T. Phare, S. P. Roberts, and M. Lipson, "On-chip platform for a phased array with minimal beam divergence and wide field-of-view," *Opt. Exp.*, vol. 26, no. 3, pp. 2528–2534, Feb. 2018.

[22] P. Ginel-Moreno *et al.*, "Highly efficient optical antenna with small beam divergence in silicon waveguides," *Opt. Lett.*, vol. 45, no. 20, pp. 5668–5671, Oct. 2020.

[23] S. Jahani and Z. Jacob, "Transparent subdiffraction optics: Nanoscale light confinement without metal," *Optica*, vol. 1, no. 2, pp. 96–100, Aug. 2014.

[24] M. B. Mia, S. Z. Ahmed, I. Ahmed, Y. J. Lee, M. Qi, and S. Kim, "Exceptional coupling in photonic anisotropic metamaterials for extremely low waveguide crosstalk," *Optica*, vol. 7, no. 8, pp. 881–887, Aug. 2020.

[25] A. Khavasi, L. Chrostowski, Z. Lu, and R. Bojko, "Significant crosstalk reduction using all-dielectric CMO-compatible metamaterials," *IEEE Photon. Technol. Lett.*, vol. 28, no. 24, pp. 2787–2790, Dec. 2016.

[26] Y. Yang *et al.*, "Crosstalk reduction of integrated optical waveguides with nonuniform subwavelength silicon strips," *Sci. Rep.*, vol. 10, no. 1, 2020, Art. no. 4491.

[27] A. Yariv, "Coupled-mode theory for guided-wave optics," *IEEE J. Quantum Electron.*, vol. 9, no. 9, pp. 919–933, Sept. 1973.

[28] S. W. Chung, H. Abediasl, and H. Hashemi, "A monolithically integrated large-scale optical phased array in silicon-on-insulator CMOS," *IEEE J. Solid-State Circuits*, vol. 53, no. 1, pp. 275–296, Jan. 2018.

[29] W. Fuscaldo, D. R. Jackson, and A. Galli, "A general and accurate formula for the beamwidth of 1-D leaky-wave antennas," *IEEE Trans. Antennas Propag.*, vol. 65, no. 4, pp. 1670–1679, Apr. 2017.

[30] X. Sun, L. Zhang, Q. Zhang, and W. Zhang, "Si photonics for practical LiDAR solutions," *Appl. Sci.*, vol. 9, no. 20, 2019, Art. no. 4225.

[31] C. P. Hsu *et al.*, "A review and perspective on optical phased array for automotive LiDAR," *IEEE J. Sel. Topics Quantum Electron.*, vol. 27, no. 1, pp. 1–16, Feb. 2021.

[32] W. L. Stutzman and G. A. Thiele, *Antenna Theory and Design*, 2nd ed., New York, NY, USA: Wiley, 1997.

[33] Y. Wang *et al.*, "2D broadband beamsteering with large-scale MEMS optical phased array," *Optica*, vol. 6, no. 5, pp. 557–562, May 2020.

[34] G. Luo *et al.*, "Demonstration of 128-channel optical phased array with large scanning range," *IEEE Photon. J.*, vol. 13, no. 3, Jun. 2021, Art. no. 6800710.

[35] L.-M. Leng, Y. Shao, P.-Y. Zhao, G.-F. Tao, S.-N. Zhu, and W. Jiang, "Waveguide superlattice-based optical phased array," *Phys. Rev. Appl.*, vol. 15, no. 1, Jan. 2021, Art. no. 014019.

[36] G. T. Reed, G. Mashanovich, F. Y. Gardes, and D. J. Thomson, "Silicon optical modulators," *Nature Photon.,* vol. 4, no. 8, pp. 518–526, Jul. 2010.

[37] G. Kang *et al.*, "Silicon-based optical phased array using electro-optic *p-i-n* phase shifters," *IEEE Photon. Technol. Lett.*, vol. 31, no. 21, pp. 1685–1688, Nov. 2016.

[38] S.-H. Kim *et al.*, "Thermo-optic control of the longitudinal radiation angle in a silicon-based optical phased array," *Opt. Lett.*, vol. 44, no. 2, pp. 411–414, Jan. 2019.